Pulsed stimuli entrain p53 to synchronize single cells and modulate cell-fate determination

Harish Venkatachalapathy[1], Zhilin Yang[2], Samira M. Azarin[1], Casim A. Sarkar[3,*], and Eric Batchelor[4,*,+]

1. Department of Chemical Engineering and Materials Science, University of Minnesota, Minneapolis, MN 55455, USA

2. Laboratory of Cell Biology, National Cancer Institute, National Institutes of Health, Bethesda, MD 20892, USA

3. Department of Biomedical Engineering, University of Minnesota, Minneapolis, MN 55455, USA

4. Department of Integrative Biology and Physiology, University of Minnesota, Minneapolis, MN 55455, USA

* Corresponding authors

+ Lead contact

Correspondence: ebatchel@umn.edu (E.B.); csarkar@umn.edu (C.A.S.)

Abstract

The dynamic expression pattern of the tumor suppressor p53 can have significant cell-to-cell heterogeneity, leading to variability in cellular stress responses and resulting in clinical consequences such as cancer chemoresistance. Using a combination of mathematical modeling, time-lapse fluorescence microscopy, and single-cell tracking, we exploit the oscillatory nature of the p53 response to DNA double-strand break (DSB) induction to reduce cellular heterogeneity by entraining p53 dynamics. Our study demonstrates that oscillatory p53 dynamics can be experimentally entrained over a wider range of DSB frequencies than predicted by an established computational model for this system. Non-intuitively, we determined that recapitulating this increased entrainment range required a modified model with a less robust oscillator and wider steady-state valley on the energy landscape. Further, we show that p53 entrainment can lead to altered expression dynamics of downstream targets responsible for cell fate in a manner dependent on target mRNA stability. Overall, this study exemplifies the potential of externally entraining p53 dynamics to reduce cellular variability and synchronize cell-fate responses to genotoxic agents.

Introduction

The tumor suppressor p53 is a central node in regulating the cellular response to various stresses.[1,2] In cancer, p53 function is crucial to the efficacy of DNA damage-inducing clinical interventions, and consequently, defects in the p53 pathway can lead to a refractory tumor response.[3–5] Interestingly, however, an intact p53 response does not guarantee a favorable outcome. Stochastic cell-to-cell variation in p53 dynamics can lead to different cell fate outcomes under the same external cue such as fractional survival under chemotherapy, even in genetically identical cells.[6–11] Clinically, these surviving cells are representative of residual disease post-treatment, posing a significant challenge to progression-free survival in patients. While this has been partly addressed by combination therapies, the interplay between heterogeneous p53 dynamics and the treatment schedule can also affect the tumor response.[12,13] Thus, there is a need for treatment strategies focused on mitigating single-cell heterogeneity in p53 dynamics to facilitate more thorough tumor elimination.

The most common example of externally driven reduction in cell-to-cell heterogeneity in dynamics is the synchronization of biological rhythms through entrainment.[14] Notably, circadian oscillations coordinate synchronous periodic behavior across multiple systems in an organism in response to 24-hour light-dark cycles.[15–17] In the absence of this periodic stimulus, there is emergent asynchrony in the oscillators due to biological noise. Interestingly, such asynchrony is characteristic of p53 expression dynamics in response to DNA double-strand breaks (DSBs). In response to DSBs produced by stressors including γ-irradiation and the radiomimetic drug neocarzinostatin (NCS), p53 levels increase and decrease in an oscillatory pattern with an average period of ~5.5 h in mammalian cells; however, the oscillations show high variability in pulse frequency between individual cells as well as time between pulses in an individual cell.[18] Similarly

variable oscillations in glycolytic networks[19] and NF-κB[20,21] have been shown to synchronize under periodic stimuli. We sought to determine if periodic DSB induction could improve synchrony in p53 oscillations (**Figure 1A**).

Using a mathematical model of the p53 response to NCS-induced DSBs developed by Mönke et al.[22], we predicted the existence of entrainment in an interval around the natural p53 pulsing period. We validated the prediction experimentally using live-cell fluorescence microscopy and single-cell tracking, demonstrating increased synchronization of p53 dynamics in response to a periodic damage signal. Surprisingly, we experimentally observed entrainment across a wider range of stimuli periods than was computationally predicted. Using parameter sensitivity analysis, we found non-intuitively that the increased entrainment range required a modified p53 DSB response model exhibiting less robust oscillations. Finally, we showed that the change in p53 pulsing period due to entrainment translates to alteration in downstream target mRNA expression dynamics for cell-fate regulatory genes.

Results

The p53 response is entrainable through periodic DSB induction

To identify whether entrainment of p53 pulses through periodic DSB induction was theoretically feasible, we used a mathematical model of the p53 DSB response calibrated using MCF-7 breast cancer cells[22] (**Figure 1B**) to simulate repeated DSB induction through the radiomimetic drug NCS and analyzed the subsequent p53 response. From deterministic simulations using an NCS-induced birth rate of b_s = 200 breaks/h, we found a small region around the natural frequency of the system (~1/5.5 h^{-1}) where p53 had the same frequency as the input DSB waveform (phase-locked) (**Figure 1C**). We validated this by calculating the entrainment score[21], which is defined as the fraction of

total power on the Fourier spectrum that corresponds to the input frequency and its harmonics. Since an entrained system would have the same frequency as the input, its corresponding frequency spectrum is expected to show high power at the input frequency and harmonics and low power elsewhere, leading to an entrainment score close to 1. Indeed, this was close to 1 for the regions in which the system was phase-locked, further validating our hypothesis that p53 can be entrained by repeated DSB induction (**Figure 1C**). This did not change significantly as a function of b_s over a range of 50 – 1000 breaks/h (**Figure S1**). Additionally, under noisy DSB dynamics, the entrainment score of an ensemble of 1,000 simulations per input frequency closely followed that of the deterministic system (**Figure 1C**), implying DSB stochasticity was likely not a significant source of variability in entrainment in the conditions analyzed.

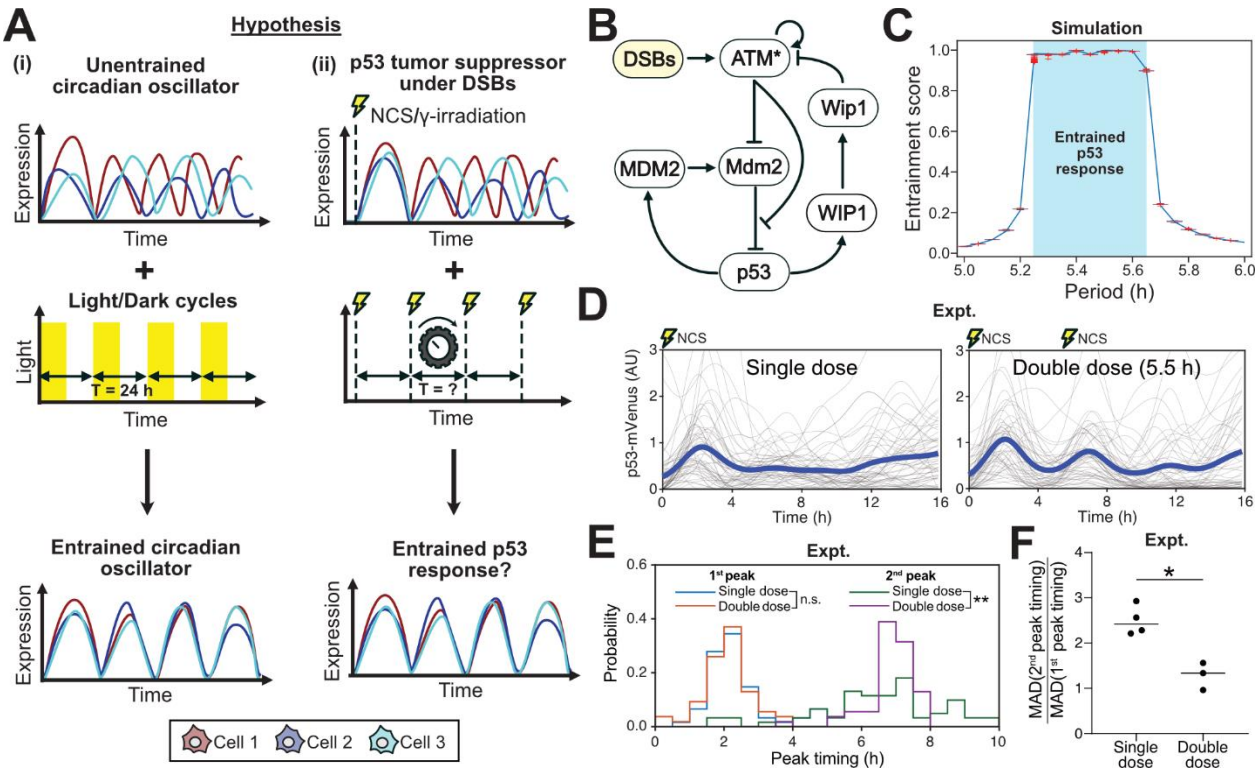

Figure 1: p53 DSB response is entrainable (A) Schematic showing asynchronous oscillations in expression levels of a (i) circadian oscillator that are synchronized under periodic light/day cycles. (ii) We hypothesized that asynchronous p53 oscillations under DSBs could be similarly entrained and synchronized under periodic DSB induction. **(B)** Diagram of the p53 regulatory network under DSBs.[22] Yellow boxes denote species with stochasticity. **(C)** Entrainment score of deterministic simulations driven by either deterministic (blue line) or stochastic (box plots, 1000 realizations) DSB dynamics. Phase-locked regions in deterministic systems indicated in cyan. **(D)** Single-cell

traces (gray) and mean (dark blue) p53-mVenus transgene expression under a single dose of NCS (400 ng/mL) or two doses spaced 5.5 h apart. **(E)** Probability distributions of first and second peak timing. (* $p < 0.05$; ** $p < 0.01$; Kolmogorov-Smirnov test) **(F)** Ratio of median absolute deviation (MAD) in peak timing of the second peak to the first, measured across four and three biological replicates for the single dose and double dose conditions, respectively. Statistical analysis presented here is from an ANOVA followed by multiple comparisons that was performed on the dataset presented in **Figure S2**.

To validate the computationally predicted conditions of entrainment, we quantified p53 dynamics in p53-mVenus expressing MCF-7 cells that were treated with either a single dose of 400 ng/mL NCS or two doses spaced 5.5 h apart (**Figure 1D**). Both conditions showed a synchronized first pulse of p53 accumulation after treatment, with no statistically significant differences in peak timing distributions (**Figure 1E**). However, the cells that received a single dose of NCS lost synchrony by the second p53 pulse, while cells that received a second dose of NCS at 5.5 h had a significantly narrower second peak timing distribution ($p < 0.01$) (**Figure 1E**). This was further validated by the smaller increases in the median absolute deviation (MAD) of second peak timing over first peak timing (single dose median: 2.41, double dose median: 1.33; $p < 0.05$) (**Figure 1F**). Overall, cells that had been treated twice with NCS better retained p53 peak timing synchrony.

p53 pulses can be entrained over a wider range of stimulus periods than predicted

To experimentally validate the computationally predicted range of stimulus periods across which entrainment is possible, hereafter referred to as entrainability, we treated the MCF-7 p53-mVenus cell line with either a single dose of 400 ng/mL of NCS or two doses spaced 3.0 h – 7.0 h apart, with a resolution of 0.5 h (**Figure 2A, Figure S2**). In contrast to model predictions of a narrow entrainment range of 5.25 h to 5.65 h, we observed statistically significant increases in synchrony in conditions with two doses spaced 4.0 h to 5.5 h apart when compared to a single dose (**Figure 2B**). We did not observe similar synchronization in the 3.0 h, 3.5 h, 6.0 h, 6.5 h, and 7.0 h

conditions. Interestingly, the 3.0 h and 3.5 h conditions did not exhibit a synchronous first pulse as typically expected. Instead, we observed cells with either two small pulses spaced close together or one big pulse spanning the approximate duration of the small pulses, thereby exacerbating heterogeneity in the p53 response in comparison to a single dose (**Figure S2**). In contrast, the 6.0 h, 6.5 h, and 7.0 h conditions exhibited a synchronized first pulse similar to a single dose of NCS but were followed by a less synchronized second pulse suggesting loss of entrainment. Surprisingly, inclusion of stochastic mRNA dynamics in computational simulations, a feature shown to widen the entrainment range in other systems[20,21,23], did not improve entrainability in our p53 model (**Figure S3)**. Taken together, these results indicate that the p53 DSB response is more entrainable than predicted and that the improved entrainability is likely not driven by intrinsic noise.

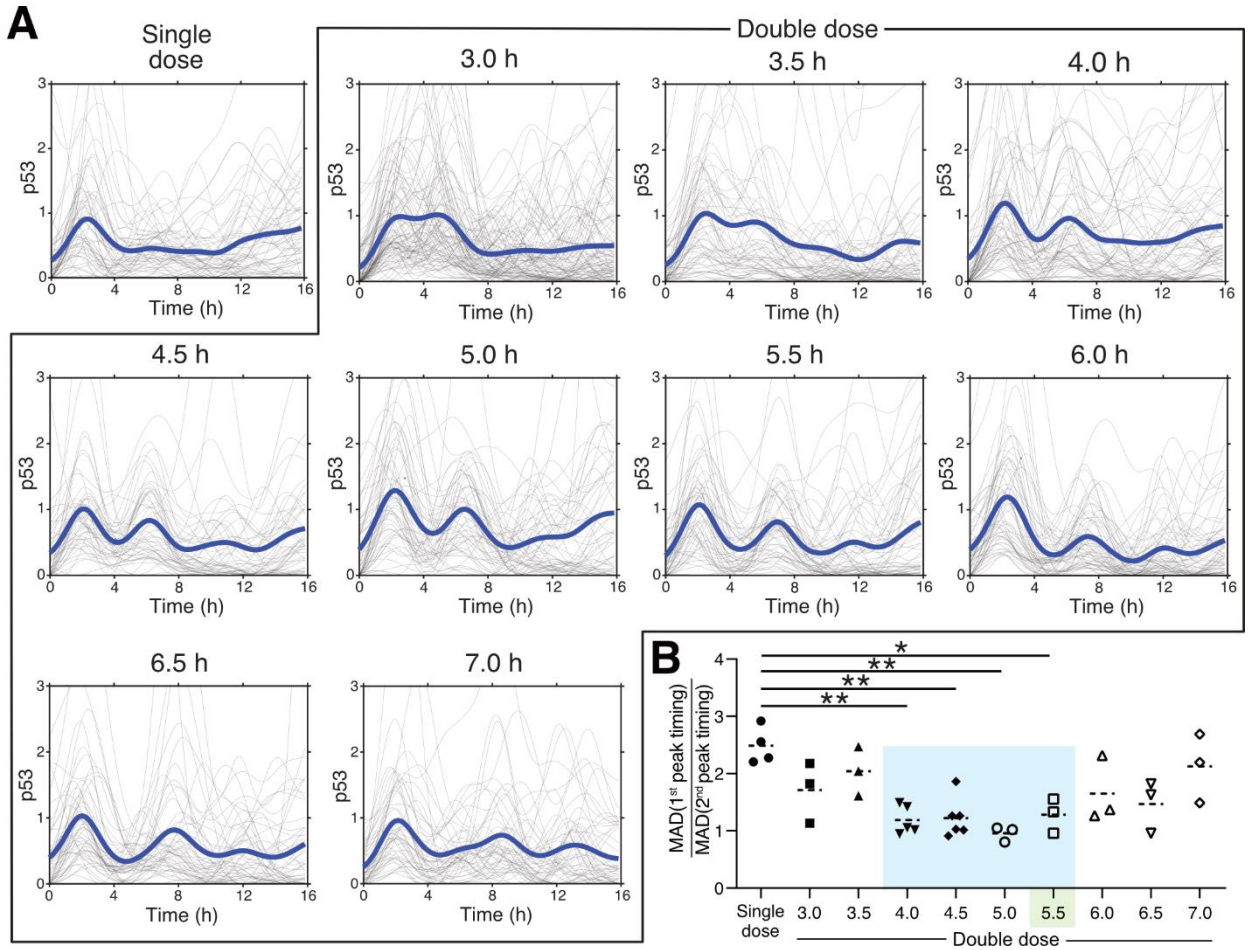

Figure 2: p53 is experimentally entrainable across a wider range of stimulus frequencies than computationally predicted (A) Single cell traces (gray) and mean (dark blue) p53-mVenus expression under a single dose of NCS (400 ng/mL) or two doses spaced 3.0 h to 6.0 h apart. Traces representative of a minimum of three biological replicates. **(B)** Fold-change in median absolute deviation (MAD) in peak timing from the first peak to the second, measured across a minimum of three biological replicates (* $p < 0.05$; ** $p < 0.01$; ANOVA followed by multiple comparisons). Single dose and 5.5 h double dose data same as **Figures 1, S2**.

Parameter sensitivity analysis identifies oscillation strength as a predictor of entrainment range

Given that intrinsic noise alone was not explanatory of the entrainment range observed experimentally, we performed a parameter sensitivity analysis to examine whether changes in system parameters could explain the experimentally observed range (**Figure 3A**).

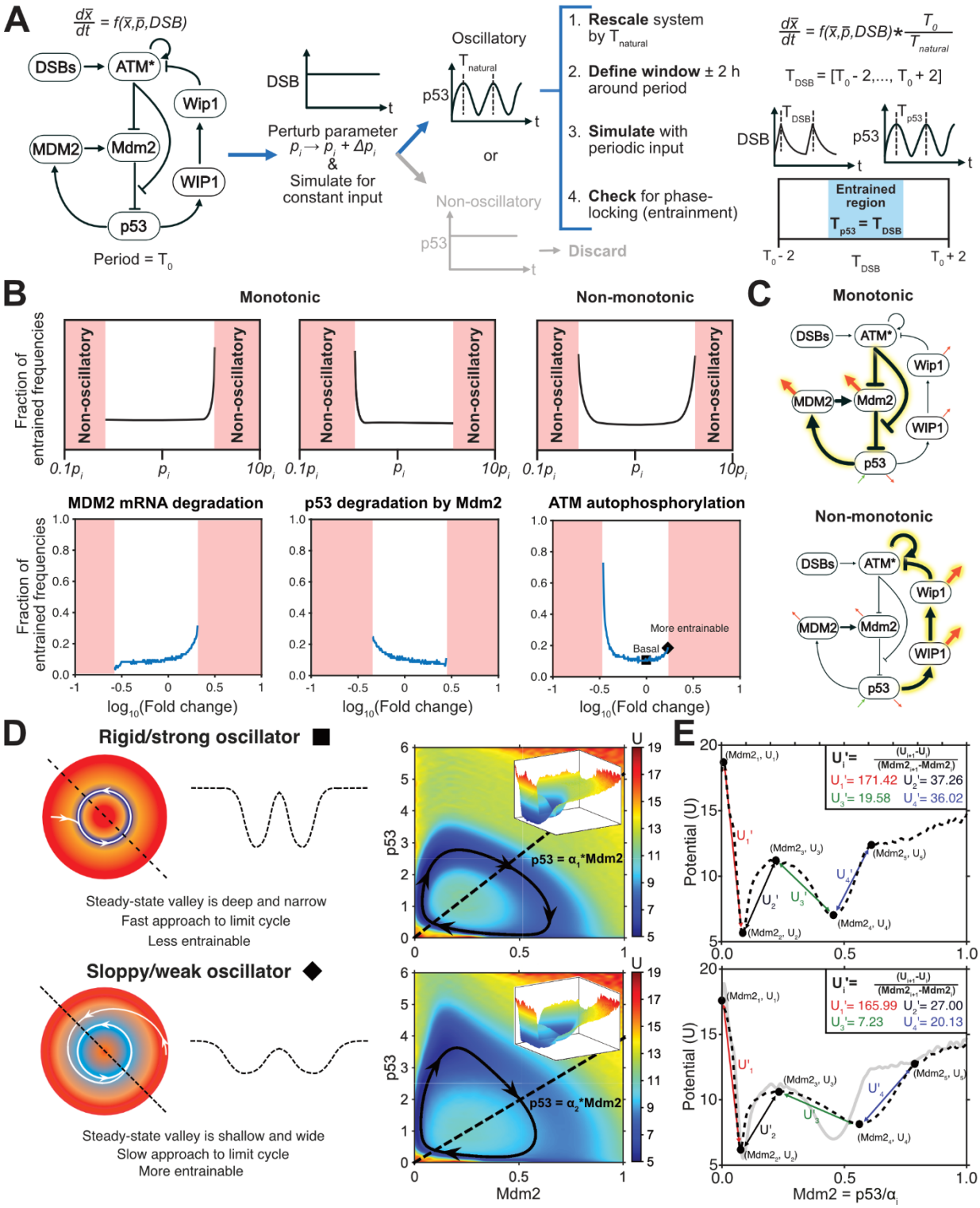

Figure 3: Parameter sensitivity analysis identifies proximity to non-oscillatory regimes and limit cycle rigidity as a positive predictor of entrainment range (A) Schematic depicting the parameter sensitivity analysis workflow. **(B)** Depictions of the two types of entrainment range responses to parameter changes in the system with examples of each type. **(C)** Schematic of the p53 DSB response model with specific interactions that exhibit monotonic or non-monotonic responses highlighted and enlarged in size. Black arrows depict interactions while green and red arrows represent basal production and degradation, respectively. **(D)** Graphical depictions and the underlying energy landscapes of a more rigid, less entrainable oscillator (basal system; black square in ATM autophosphorylation rate

diagram in (B)) and less rigid, more entrainable oscillator (ATM autophosphorylation rate changed to 1.67 times the basal value; black diamond in ATM autophosphorylation rate diagram). Rigidity refers to the strength of the limit cycle attractor. Black line represents the deterministic path (limit of zero noise) and arrows represent direction of movement. Dashed line represents the line passing through the origin and the inner maximum of the steady-state valley described by Mdm2 = α_i*p53 where α_1 = 4.76 and α_2 = 4.24. Energy landscapes generated using p53 DSB model with stochastic DSB and mRNA dynamics and system size of 100. **(E)** Slice of energy landscapes corresponding to (D) along the dashed line depicting the change in the rigidity of the steady state. Gray line in the bottom panel corresponds to the more rigid landscape (dashed line in the top panel).

We observed two classes of behavior based on whether the range of input frequencies where entrainment was possible changed monotonically or non-monotonically with the parameter. The monotonic class consisted of parameters associated with the p53-Mdm2 loop (e.g., MDM2 mRNA degradation rate and Mdm2 mediated p53 degradation rate). The non-monotonic class consisted of parameters associated with the p53-Wip1-ATM* interactions (e.g., ATM autophosphorylation rate) (**Figure 3B, C**). While some parameters had a stronger effect on entrainability than others (**Figure S4**), the most striking feature was a sharp increase in entrainment range at the cusp of the transition to a non-oscillatory regime in some cases, implying that less robust oscillatory behavior improved entrainment. That is, the range of entrainable frequencies was largest in parameter regimes where small changes in parameters such as those arising from extrinsic noise, a part of natural biological variability, led to the loss of oscillatory behavior. While it is non-intuitive that entrainment, a feature associated with oscillations, correlated with less robust oscillations, we hypothesized that an endogenous oscillator with a weaker limit cycle attractor would be more susceptible to perturbations and thereby more entrainable by an external cue. To validate this, we used a trajectory-based energy landscape methodology[24,25] to generate the underlying energy landscapes for the basal system and compared it to a more entrainable system (1.67 times the basal ATM autoactivation rate). We expected oscillators with weaker (less rigid) limit cycle attractors to have a shallower stable steady-state valley that is reflective of higher susceptibility to external perturbations while oscillators with stronger (more rigid) limit cycle

attractors would have a deeper valley (less affected by external forces) (**Figure 4D**). By comparing the two landscapes, we found that the valley around the mean system path in the more entrainable system was wider and had a gentler gradient around it (**Figure 4E**). This was further corroborated by examining the potential across a line connecting the origin and the inner maximum within the circular steady-state valley. This showed higher stable steady-state potentials and lower slopes around the states in the more entrainable landscape, two characteristics that suggest greater responsiveness to external cues. Taken together, the results validate our hypothesis that a less rigid oscillatory system is more affected by external perturbations and thus is more entrainable and that the p53 DSB response needs to be underpinned by such a weak oscillator to recapitulate our experimental observations.

p53 pulse modulation through entrainment changes downstream mRNA target dynamics in a half-life-dependent manner

As p53 dynamics control cell fate under DSBs, we hypothesized that changes in p53 pulsing frequency due to entrainment alter the downstream response. We validated this by examining the expression of the cell-cycle inhibitor p21, a canonical p53 downstream target. Comparing the mean p53 expression level across single cells for NCS stimulus periods of 4.0 hours and 5.5 hours, we observed a shift in the peak timing of the second p53 pulse (**Figure 4A**). Using mathematical modeling, we predicted that these p53 dynamics result in higher expression of p21 at the population level between 5.0 h and 8.0 h as well as an earlier second peak in the NCS 4.0 h condition (**Figure 4B**). To validate this, we quantified p21 protein dynamics in MCF-7 cells tagged with mVenus at the p21 C-terminal genomic locus under different NCS treatment intervals (**Figure 4C**). We only considered cells that had a minimum normalized expression of $10^{0.5}$ units at $t < 3.0$ h to filter out

cell-cycle dependent delays in p21 upregulation[26]. Consistent with the model, we found higher mean p21 expression in the NCS 4.0 h condition between 4.0 h to 8.0 h compared to the NCS 5.5 h condition (**Figure 4D**). Further, we found that the second peak timing of p21 expression was later for cells administered a second dose of NCS at 5.5 h compared with 4.0 h ($p < 0.0001$; Wilcoxon rank sum test). No differences were observed in the first peak timings between the two conditions (**Figure 4E**).

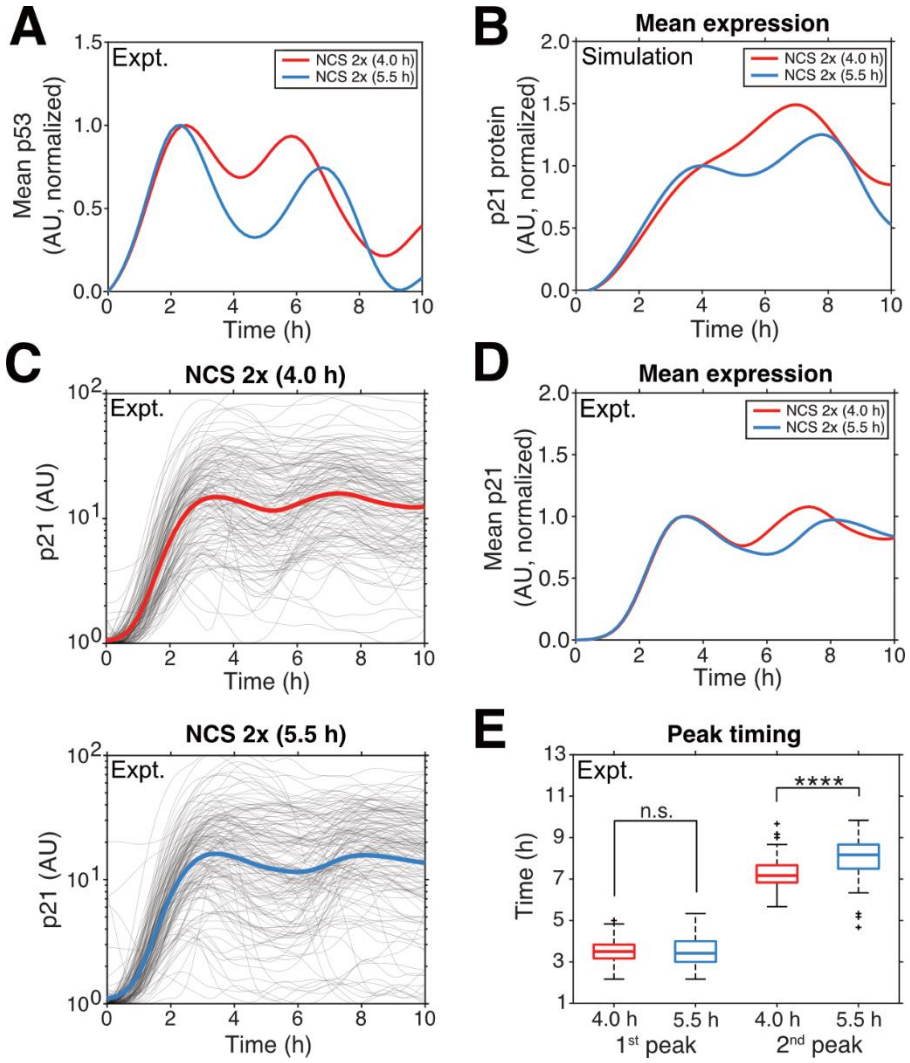

Figure 4: Entrainment of p53 pulses modulates downstream p21 expression (A) Mean p53-mVenus expression under two doses of NCS spaced 4.0 h (red) or 5.5 h (blue) apart, rescaled from 0 to 1 such that the first peak for both curves are the same height. **(B)** Model prediction of downstream p21 expression driven by p53 expression shown in (A). **(C)** Single cell traces (gray) and mean (red and blue lines) p21-mVenus expression of responding cells under the conditions in (A). **(D)** Mean p21 expression for the two conditions shown in (C). Experimentally observed curves are comparable to computationally predicted curves in (B). **(E)** Comparison of p21 peak timings for the first and second

peaks in the 4.0 h and 5.5 h conditions showing no differences for the first peak, but a later second peak for the 5.5 h condition. Comparisons were performed using Wilcoxon rank sum test (**** $p < 0.0001$).

We also observed increased mRNA expression of *CDKN1A* (p21 mRNA) as well as other p53 targets (*GADD45A*, *TRIAP1*, and *FAS*) under administration of a second dose of NCS at 4.0 h compared with 5.5 h between 5.0 h and 8.0 h (**Figure S6**). This effect was most prominent and consistent in *GADD45A*, but less so in the other genes, appearing in only one or two out of three biological replicates. This may be due to differences in mRNA stability – *GADD45A* is highly unstable and follows p53 dynamics more closely in comparison to more stable species such as *CDKN1A*, *TRIAP1*, and *FAS*.[27] Therefore, any changes in p53 dynamics would be better reflected in *GADD45A* dynamics as opposed to more stable downstream mRNA targets. Indeed, mathematical modeling of mRNA transcription using p53 dynamics from **Figure 4A** as an input, we find that less stable mRNA targets show higher differences in expression between the 4.0 h and 5.5 h NCS interval treatments (**Figure S7**). Overall, this suggests that entrainment of the single-cell p53 response can modulate downstream target expression in a target stability-dependent manner.

Discussion

Heterogeneous p53 dynamics can drive survival of some cancer cells despite significant cell death in the overall tumor mass, eventually resulting in cancer recurrence even with combination therapies designed to circumvent the effects of such heterogeneity. Inspired by the synchronization of circadian rhythms[15–17], NF-κB oscillations[20,21], and glycolytic oscillations[19] under a periodic external cue, we engineered increased cell-to-cell synchrony in the p53 response through entrainment using repeated DSB induction by periodic doses of NCS, a small molecule radiomimetic. This synchronous population is expected to have a more uniform response to

external perturbations such as chemo- or radiotherapy, providing a critical proof of principle for potential applications in reducing one possible source of heterogeneity in cancer therapies. Further studies can build upon our current findings to identify efficacious sources and timings of therapeutic perturbations.

In addition to the synchronizing effects of entrainment on p53 dynamics, the change in p53 pulse frequency by entrainment altered downstream target dynamics in a mRNA degradation rate-dependent manner at both the population level and the single-cell level. While this was most obvious when examining p21 cell cycle arrester expression at the single-cell level (**Figure 4B-E**), the global effects on the p53 target transcriptome were less clear. Out of four downstream targets examined, only the least stable species *GADD45A* reproducibly displayed altered expression dynamics at the population level. The effect of entraining treatments was only qualitatively, but not statistically, reproducible in the more stable targets (**Figure S6**) including *CDKN1A* (p21 mRNA) which had exhibited stimulus frequency-dependent dynamics at the single-cell level. Mathematical modeling attributed this lack of statistical significance to a diminished difference in mRNA dynamics between the two entraining frequencies for more stable targets, which were likely more difficult to recapitulate experimentally due to natural biological variability, especially with bulk measurements of a non-homogeneous population (**Figure S7**). Overall, these findings imply that less stable p53 targets, such as those involved with DNA repair and cell cycle arrest[27–29], are most likely to be affected by stimulus frequency. This insight could be used to identify optimal treatment intervals that differentially regulate cell-fate specific genes and potentially achieve a specific cell fate in therapy design. For instance, cancer cells could be biased towards apoptosis over senescence to avoid negative effects of senescence such as inflammation that damages the surrounding healthy tissue. Finally, due to the use of a γ-irradiation analog, the

strategies outlined herein could be more directly translated to a clinical context without concern for pharmacokinetic and pharmacodynamic effects that typically need consideration in combination drug-based therapies.

However, as seen with p21 protein expression (**Figure S5**), heterogeneity in cell state can lead to divergent cell fate responses despite similar p53 dynamics.[26] Therefore, further investigation is required to understand the specific effects of cell state heterogeneity in this context and develop strategies for combating these effects. Additionally, long-term dynamics of the entrained p53 system, on the order of days, should be quantified to determine the effects on cell fate regulation. In response to entrainment, it is not known whether p53 remains oscillatory[30] or if there may be an eventual transition to different dynamics such as elevated but non-oscillatory p53.[31] Furthermore, the effects of entrainment on long-term cell fate regulation require investigation as it has been shown that entrained and unentrained systems can have different gene expression profiles, as seen in the case of NF-κB.[20]

Interestingly, the range of entrainment observed experimentally (> 1.5 h) (**Figure 2A, B**) was significantly larger than computationally predicted (~0.5 h) even under high DNA damage (**Figure 1C, Figure S1**). Further, in contrast to other systems where intrinsic noise widens the entrainment range[20,21,23], there was no such intrinsic noise-driven entrainment range widening in the p53 system. Instead, using parameter sensitivity analysis, we found that the widened entrainment range in the p53 system is due to the presence of a less rigid endogenous oscillator than predicted by the mathematical model. In other words, a landscape that permitted more uniform cell behavior through entrainment was characterized by a wider stable steady state valley under a constant input, a feature associated with more heterogeneity. This phenomenon has also been observed in the circadian system.[32,33] While this seems counterintuitive, it is consistent with

the expected behavior of weak attractor which permits significant noise-driven deviations from the mean under steady state, a key feature of p53 oscillations under DSBs[30,35], and is simultaneously more malleable to an external cue, thereby allowing a more uniform response under perturbations. Taken together, these observations suggest that the p53 dynamics under DSBs are governed by a weak oscillator. However, it is unclear whether this can be simply recapitulated by reparameterization of the model or if it requires the addition of missing regulatory loops or species. For example, incorporating bidirectional regulation of DSB repair and p53 could lead to better entrainment if there is a rigidity mismatch between DSB generation/repair and p53 oscillations.[34]

Overall, this study exemplifies the potential of entraining p53 dynamics through tailored administration of a genotoxic agent to attenuate single-cell heterogeneity. This entrainment also led to stimulus frequency-dependent modulation of downstream target genes responsible for cell fate determination. Future work focused on utilizing the reduced single-cell heterogeneity as well as differential gene expression demonstrated here can aid in the design of more effective therapeutic strategies to promote recurrence-free survival.

Materials and Methods

Mathematical modeling of p53 dynamics

Deterministic simulations were carried out in MATLAB (Mathworks, Natick, MA, USA), and stochastic simulations were carried out using the Gillespie algorithm32 in C++. A mathematical model of the p53 response under double stranded DNA breaks (DSBs) developed by Mönke et al.[22] was used in all simulations, with modifications as specified. The mRNA synthesis rates of MDM2 and WIP1 were increased by 20% each (from 1.0 AU/h to 1.2 AU/h) to reduce the observed

p53 pulse frequency from once every 7.0 h to once every 5.5 h, matching the expected period in MCF-7 cells.[35] Other parameters could also be potentially varied to get this same effect. We chose MDM2 and WIP1 production rates based on the sensitivity analysis by Mönke et al.[22] Additionally, the functional form of DSB sensing by ATM, *f(DSB)* (**Figure S8A**), was changed from a saturable equation, $f(DSB) = DSB/(\gamma + DSB)$, to a non-saturable one, $f(DSB) = log(DSB/\gamma + 1)$, to reflect the shift from oscillatory to sustained p53 dynamics observed experimentally under high DNA damage.[36] Both of these functions show very similar behavior for small numbers of DSBs (**Figure S8B**). However, the saturable function approaches a maximum of 1 and continues to drive oscillatory behavior for large numbers of DSBs (**Figure S8C**). In contrast, the non-saturable log function causes a shift from oscillatory to sustained p53 dynamics under high damage (**Figure S8D**). Values for all rate constants used are provided in **Table S1**.

Deterministic model

The double stranded break and repair process from the original model[22] was changed from a discrete stochastic birth-death process to a deterministic equation: $d(DSB)/dt = b - r*DSB$. Following Mönke et al.[22], for the first hour after NCS treatment, the birth rate was changed to b_s, a parameter proportional to the NCS concentration. After one hour until further damage was inflicted, the birth rate reverted to a basal birth rate b_b = 2.3 breaks/h. Additionally, DSBs were repaired with a constant death rate $r = 0.315\ h^{-1}$ throughout the simulation. For repeated treatment, this resulted in a sawtooth-like waveform where there was nearly linear accumulation of DSBs with a slope proportional to b_s for 1 hour followed by exponential decay (**Figure 7E**). Simulation files are provided in **File S1**.

Stochastic model

The model included two key sources of noise: (1) DSB birth-death process, and (2) mRNA production and degradation. Due to its independence from the rest of the model, noise due to stochastic DSB generation and repair was implemented by separately generating the appropriate waveform using the Gillespie method[37], and then feeding this waveform as a piecewise function of time into the time-stepping algorithm. The mean of the DSB process realizations closely followed the sawtooth-like deterministic shape (**Figure S8F**). The model with DSB noise was simulated in MATLAB R2020a using the *ode23s* function with the DSB waveform input as a piece-wise function such that for $t_i < t < t_{i+1}$, $DSB = DSB_i$, where DSB_i is the number of double-strand breaks as per the stochastic birth-death model. To include noise from the stochastic production and degradation of mRNA species (WIP1 and MDM2), we implemented a hybrid stochastic-deterministic simulation in C++. In this implementation, the equations for WIP1 and MDM2 mRNAs were solved using the Gillespie method and all other equations were solved deterministically using discrete time steps between each time step of the Gillespie algorithm. The number of time steps was chosen to have a smaller average time step duration than the DSB noise only simulation from MATLAB. The number of DSBs were updated according to the pre-generated waveform such that $DSB = DSB_i$ when $t > t_i$, $DSB = DSB_{i+1}$ when $t > t_{i+1}$, and so on. Each stochastic simulation was run 1,000 times, as determined by the convergence in entrainment score (**Figure S8G**). Simulation files are provided in **File S1**.

Entrainment characterization

For deterministic simulations, the system was considered phase-locked and therefore entrained if, at steady state, the period was within 0.1% of the input period (an order of magnitude lower than

the period grid size/interval when evaluating entrainment). Due to variability in the period of oscillation in stochastic systems, this approach was not applied there. Instead, the degree of entrainment was calculated using the entrainment score (*E*), following the procedure used by Gupta et al.[21] Briefly, this score is the fraction of power at the input frequency and its harmonics, compared to the entire frequency spectrum as calculated by a one-sided discrete Fourier transform (DFT, custom script in MATLAB). The DFT calculates power *P* at a set of frequencies *f* dependent on trajectory length and discretization. Due to finite observation time, we will have a finite number of frequencies which may or may not include the exact input frequency and the corresponding harmonics. Instead, the spectral power of the system will be spread around the components of the DFT that are near the exact frequencies. In consideration of this numerical issue, we used a frequency window *w*, that was 1% of the width of the natural frequency of the system $f_{natural}$ within which the corresponding power for each frequency was calculated. The entrainment score was then calculated as follows,

$$E = P_{in}/P_{total} \tag{1}$$

where,

$$P_{in} = \sum_{i}\sum_{k} P(f_k : (\, i * f_{in} - w) \leq f_k \leq (i * f_{in} + w)) \tag{2}$$

$$P_{total} = \sum_{k} P(f_k) \tag{3}$$

$$w = 0.01 * f_{natural} \tag{4}$$

f_k is the kth frequency of the DFT, *i* is an integer corresponding to the ith harmonic, f_{in} is the input

frequency, w is the window size around the frequencies of interest, and $f_{natural}$ is the natural frequency of the system.

All simulations were run for 5,000 hours for entrainment characterization. As opposed to shorter times, this duration exhibited minimal fluctuation in the entrainment score in phase-locked regions (**Figure S8H**). These fluctuations are artifacts caused by the finite numerical nature of the DFT, as explained in the previous paragraph.

Parameter analysis for system entrainment

Overview

Parameters were varied, one at a time, and the resulting system was classified as oscillatory or non-oscillatory based on the total Fourier power of the normalized waveform. The system was then rescaled by multiplication with 5.5 (natural period of the basal system) and division with the natural period of the modified system. Entrainment, as defined by phase-locking, was examined in a window of ± 2 h around the natural pulsing frequency of the system.

Parameter variation

Simulations of the fully deterministic system were used to characterize the effect of individual parameters on entrainment. Each parameter was separately varied in a 10-fold range below and above the default value in increments of 0.005 on the $\log_{10}$ scale.

Constant DSB simulation and classification into oscillatory/non-oscillatory

The system was first simulated for a constant DSB input of 200 for t = 5,000 h. The p53 trajectory after 1,000 h (in intervals of 0.05) was classified as oscillatory or non-oscillatory based on the total

power on the Fourier spectrum. The trajectory was first rescaled linearly from 0 to 1 (*rescale* function in MATLAB) to remove variability in power due to amplitude and then was used to calculate the one-sided DFT. If the total power of the DFT was > 0.2, it was classified as oscillatory. This threshold was determined by simulating 1,000 Latin-hypercube sampled parameters in a 2-fold range, for constant DSB inputs from 0 to 1,000 in increments of 20, and examining the distribution of total power (**Figure S8I**). A clearly bimodal distribution arose: one population of trajectories had a minimum power of 0.2, likely representing oscillatory cases, while the other population had a maximum power of ~0.1, corresponding to non-oscillatory cases. A few randomly selected trajectories from both parts of the distribution were visually inspected to validate this. Non-oscillatory cases were discarded while oscillatory cases moved on to the next stage.

System rescaling with natural period

Oscillatory systems were then rescaled by multiplying the right-hand side of the differential equation expressions by 5.5 h (natural period of the basal system) and dividing it by the natural period of the oscillatory system (in h). This ensures commensurate comparisons of entrainment ranges across different parameter sets where the system may have different natural periods.

Entrainment curve generation and characterization

The natural period of the oscillatory trajectory was determined by the most prominent peak on the DFT. A window (± 2 h, in increments of 0.05 h) was defined around this period and entrainment was characterized for periodic inputs by examining phase-locking within this region. The effect of each parameter on entrainment was examined by the number of points entrained for each parameter

value divided by the total number of points in the window.

Mathematical modeling of downstream targets

p21 protein dynamics in **Figure 4B** were simulated using a mathematical model of p21 mRNA and protein dynamics developed by Reyes et al.[30] All rate constants were the same as the original publication except for K_0 (Michaelis constant of p53-dependent p21 transcription) which was set to 0.67. This was done to account for the differences in the scaling of p53 traces between this work and Reyes et al.[30] General mRNA dynamics in **Figure S7** were obtained using a standard p53-dependent transcription model with p53 levels from **Figure 4A** rescaled from 1 to 5 as the input, consistent with Porter et al.[27] Rate constant values were the same as the original work. Simulation files are provided in **File S1**.

Cell culture

MCF-7 cells transfected with p53-mVenus and H2B-Cerulean were maintained in RPMI-1640 media supplemented with 10% (v/v) FBS and 1% (v/v) Pen-Strep (all reagents from Life Technologies) in a humidified incubator at 37 °C and 5% CO_2. MCF-7 cells with p21 tagged fluorescently at the endogenous genomic locus (a kind gift from Sabrina L. Spencer[38]) were maintained in the same medium. Due to the loss of DHB-mCherry (Cdk2 sensor) and/or H2B-mTurquoise (nuclear marker) in subpopulations of these cells, fluorescence-activated cell sorting (FACS) using a BD FACSAria II instrument was used to obtain cells that retained expression of both constructs.

Fluorescent clonal cell line generation for live-cell imaging of p53 expression

Lentiviral particles containing pLentiPGK-Hygro-DEST-H2B-mCerulean3 (kind gift from Markus Covert[39]; Addgene: 90234) vector were produced in HEK293T (ATCC) cells using Lenti-X Packaging Single Shots (TakaraBio) using the manufacturer's protocol. The resulting particles were used to infect MCF-7 cells expressing a previously characterized p53-mVenus fusion.[36] Cells stably expressing both constructs were selected in cell culture media containing 50 μg/mL hygromycin and 400 μg/mL neomycin (Life Technologies). Clonal cell lines were generated by limiting dilution. Clones were then screened for the presence of Cerulean fluorescence. Additionally, the cells were validated to exhibit the previously reported pulsatile p53-mVenus expression dynamics under 400 ng/mL of neocarzinostatin (NCS; MilliporeSigma).

Live-cell imaging and single-cell tracking

For live-cell imaging, cells were plated on 96-well No. 1.5 glass-bottom dishes (Mattek) to be 60% confluent at the start of treatment. Prior to imaging, cells were washed with DPBS (1x), after which transparent RPMI-1640 media (Life Technologies) – lacking phenol red, riboflavin, and L-glutamine, and supplemented with 2% (v/v) FBS and 1% (v/v) Pen-Strep – was added. Cells were imaged with a Nikon Eclipse Ti2 inverted fluorescence microscope equipped with an automated stage (Prior) and a custom chamber to maintain 37 °C, 5% CO_2, and high humidity. Images were collected every 10 minutes for the brightfield, YFP, and CFP channels using a 20x CFI Plan Apochromat Lambda (NA=0.75) objective (Nikon). Exposure time for each channel was set to be <500 ms. The ND2 format imaging data were exported as individual tiff files for each channel, time point, and stage position using Bio-Formats[40] command line tools. Cells were tracked semi-automatically in p53Cinema[30] using the nuclear marker H2B-mCerulean in the CFP channel, agnostic to p53-mVenus expression in the YFP channel. p53-mVenus expression for each cell

track was then obtained using the getDatasetTraces_fillLineageInformation function with a sampling radius of 5 pixels applied to the YFP channel.

p53 single-cell trace processing and analysis

All p53-mVenus traces for each stage position were first divided by the mean p53-mVenus fluorescence reading at the start of the experiment ($t = 0$) at that position to account for illumination variability between stage positions. Any missing readings were replaced by the p53-mVenus expression at the previous time point within that trace (*fillmissing* function in MATLAB). The traces were then smoothed using a gaussian moving filter (*smoothdata* function in MATLAB) with a window size corresponding to a real-world time of 3 hours and 20 minutes; this window size aids in smoothing out smaller noisy fluctuations while retaining overall pulsatility of the system. The final traces were obtained by subtracting the minimum value of each trace from itself providing a lower bound at 0 for the p53 signal in each cell. The analysis script is provided in **File S1**.

Peak detection and peak-timing analysis

Peaks were detected for each trace and the mean of all traces using the *findpeaks* function in MATLAB and specifying a set number of peaks to be detected. To quantify the peak-timing variability for each nth peak, we first identified the peak in each trace that is closest to the nth peak of the mean p53 signal and then calculate the median absolute deviation in peak-timing in this set. Using this method instead of simply considering the nth peak for each trace avoids erroneous propagation of confounding effects due to cells that did not pulse during the first dose, but rather pulsed starting from subsequent doses, while still accounting for whether a cell pulsed or not. The analysis script is provided in **File S1**.

Gene expression quantification

Cells were plated on 35 mm dishes to be 60% confluent at the start of treatment. To obtain cell pellets, each dish was harvested at the specified time point by scraping in DPBS followed by centrifugation and aspiration of the supernatant. The resulting pellets were immediately stored at -80 °C. Total RNA was extracted from cell pellets using a RNeasy Mini Kit (QIAGEN). Lysis was performed using 350 µL of the provided lysis buffer and the lysate was passed through a QIAshredder column (QIAGEN). RNA from the lysate was obtained by following the manufacturer's protocol and quantified using a Nanodrop 2000 (ThermoFisher Scientific). cDNA was prepared by loading 2 µg of RNA per sample into a 20 µL reverse transcription (RT) reaction using a High-Capacity cDNA Reverse Transcription Kit (ThermoFisher Scientific) as per the manufacturer's protocol. The resulting cDNA mixture was diluted 1:5 (20 µL of cDNA added to 80 µL of nuclease-free water) before usage. A 20 µL reaction mix was prepared using 10 µL iTaq Universal SYBR Green Supermix (Bio-Rad), 1 µL 10 µM forward/reverse primer mix (sequences from Porter et al.[27]) , 8 µL nuclease-free water, and 1 µL template. qRT-PCR was then performed using a CFX Connect Real-Time PCR Detection System (Bio-Rad) with the following conditions: hot start (95 °C for 2 min), and 40 cycles of PCR (96 °C for 5 s, 64 °C for 20 s), ending in melt curve acquisition (64 °C–95 °C with 0.5 °C resolution). Melt curves (Change in relative fluorescence units per unit temperature vs. Temperature) were visually inspected for existence of a single peak to validate specific amplification for each gene. The threshold cycle count values (*Cq*) for each gene were obtained using the Bio-Rad CFX Manager 3.1 software. The fold change in expression was calculated by $2^{-\Delta\Delta C_q(X,t)}$ where $\Delta\Delta C_q(X,t)$ is defined as:

$$\Delta\Delta C_q(X,t) = \left[\bar{C}_q(X,t) - \bar{C}_q(GAPDH,t)\right] - \left[\bar{C}_q(X,0) - \bar{C}_q(GAPDH,0)\right] \qquad (5)$$

where $\bar{C}_q(X,t)$ is the mean Cq value for gene X at time t.

The error in fold-change was obtained by propagating the variability in Cq values involved in the calculation. The error in gene X at time t was obtained as follows:

$$Error(X,t) = 2^{-\Delta\Delta C_q(X,t)} * \log(2) * \sqrt{\sigma_{X,t}^2 + \sigma_{GAPDH,t}^2 + \sigma_{X,0}^2 + \sigma_{GAPDH,0}^2} \qquad (6)$$

where $2^{-\Delta\Delta C_q(X,t)}$ is the fold change and $\sigma_{X,t}^2$ is the variance in Cq of gene X at time t.

Statistical analysis

All statistical analyses were carried out using GraphPad Prism 9.0 or MATLAB. Experimental data in **Figure 1** and **Figure 2** passed a normality check using the Shapiro-Wilk test (**Figure S8J**) and were compared using one-way ANOVA followed by multiple comparison testing (Prism). Fold changes in variability for NCS 4.0 h (n = 6, originally) and 4.5 h (n = 7, originally) were run through an outlier detection test (Prism), and one data point for each condition was identified as an outlier and discarded prior to further statistical analysis. qPCR data in **Figure 4C** were analyzed using two-way ANOVA followed by multiple comparison testing (Prism). Peak timings in **Figure 4E** failed a normality check by using the Kolmogorov-Smirnov test and were therefore compared using a non-parametric Wilcoxon rank sum test (*kstest* and *ranksum* functions in MATLAB). qPCR data in **Figure S6** were analyzed on the C_q scale. The mean expression of each gene from three biological replicates was analyzed using a repeated measures ANOVA followed by multiple comparisons. Expression of each gene within a biological replicate was also individually analyzed from technical replicates using an ANOVA followed by multiple comparisons.

Data Availability

Upon acceptance of the manuscript for publication, computational code for all models will be

publicly available through GitHub, and imaging datasets will be publicly available through Image Data Resource.

Acknowledgments

The authors thank Kala Guettler for assistance with single-cell tracking. The authors also thank Sabrina Spencer for providing the p21-Cdk2 tagged cell line used in this study. This work was supported by funding from the University of Minnesota (S.M.A. and E. B.) and the National Institutes of Health (R35GM136309 to C.A.S. and R01GM149666 to E.B.), as well as access to high-performance computing resources from the Minnesota Supercomputing Institute and fluorescence-activated cell sorting services from the University Flow Cytometry Resource at the University of Minnesota.

Conflict of Interest

The authors declare no conflicts of interest.

References

1. Vousden, K.H., and Lane, D.P. (2007). p53 in health and disease. Nat. Rev. Mol. Cell Biol. 2007 84 *8*, 275–283. 10.1038/nrm2147.

2. Horn, H.F., and Vousden, K.H. (2007). Coping with stress: multiple ways to activate p53. Oncogene 2007 269 *26*, 1306–1316. 10.1038/sj.onc.1210263.

3. Bieging, K.T., and Attardi, L.D. (2012). Deconstructing p53 transcriptional networks in tumor suppression. Trends Cell Biol. *22*, 97–106. 10.1016/j.tcb.2011.10.006.

4. Lane, D.P., Cheok, C.F., and Lain, S. (2010). p53-based cancer therapy. Cold Spring Harb. Perspect. Biol. *2*. 10.1101/cshperspect.a001222.

5. Boutelle, A.M., and Attardi, L.D. (2021). P53 and tumor suppression: it takes a network. Trends Cell Biol. *31*, 298–310. 10.1016/j.tcb.2020.12.011.

6. Batchelor, E., and Loewer, A. (2017). Recent progress and open challenges in modeling p53 dynamics in single cells. Curr. Opin. Syst. Biol. *3*, 54. 10.1016/j.coisb.2017.04.007.

7. Friedel, L., and Loewer, A. (2022). The guardian's choice: how p53 enables context-specific decision-making in individual cells. FEBS J. *289*, 40–52. 10.1111/febs.15767.

8. Paek, A.L., Liu, J.C., Loewer, A., Forrester, W.C., and Lahav, G. (2016). Cell-to-cell variation in p53 dynamics leads to fractional killing. Cell *165*, 631–642. 10.1016/j.cell.2016.03.025.

9. Xie, J., Zhang, L., Liu, B., Liang, X., and Shi, J. (2022). Single-cell analysis of p53 transitional dynamics unravels stimulus- and cell type-dependent signaling output motifs. BMC Biol. *20*, 1–14. 10.1186/s12915-022-01290-7.

10. Yang, R., Huang, B., Zhu, Y., Li, Y., Liu, F., and Shi, J. (2018). Cell type–dependent bimodal p53 activation engenders a dynamic mechanism of chemoresistance. Sci. Adv. *4*. 10.1126/sciadv.aat5077.

11. Wu, M., Ye, H., Tang, Z., Shao, C., Lu, G., Chen, B., Yang, Y., Wang, G., and Hao, H. (2017). p53 dynamics orchestrates with binding affinity to target genes for cell fate decision. Cell Death Dis. *8*, e3130. 10.1038/cddis.2017.492.

12. Chen, S.-H., and Lahav, G. (2016). Two is better than one; toward a rational design of combinatorial therapy. Curr. Opin. Struct. Biol. *41*, 145–150. 10.1016/j.sbi.2016.07.020.

13. Chen, S.-H., Forrester, W., and Lahav, G. (2016). Schedule-dependent interaction between anticancer treatments. Science *351*, 1204–1208. 10.1126/science.aac5610.

14. Jiménez, A., Lu, Y., Jambhekar, A., and Lahav, G. (2022). Principles, mechanisms and functions of entrainment in biological oscillators. Interface Focus *12*. 10.1098/RSFS.2021.0088.

15. Reppert, S.M., and Weaver, D.R. (2002). Coordination of circadian timing in mammals. Nature *418*, 935–941. 10.1038/nature00965.

16. Roenneberg, T., Daan, S., and Merrow, M. (2003). The art of entrainment. J. Biol. Rhythms *18*. 10.1177/0748730403018003001.

17. Aton, S.J., and Herzog, E.D. (2005). Come together, right…now: synchronization of rhythms in a mammalian circadian clock. Neuron *48*, 531–534. 10.1016/j.neuron.2005.11.001.

18. Batchelor, E., Loewer, A., and Lahav, G. (2009). The ups and downs of p53: understanding protein dynamics in single cells. Nat Rev Cancer *9*, 371–377. 10.1038/nrc2604.

19. Gustavsson, A.K., Adiels, C.B., Mehlig, B., and Goksör, M. (2015). Entrainment of heterogeneous glycolytic oscillations in single cells. Sci. Rep. *5*, 1–16. 10.1038/srep09404.

20. Kellogg, R.A., and Tay, S. (2015). Noise facilitates transcriptional control under dynamic inputs. Cell *160*, 381–392. 10.1016/j.cell.2015.01.013.

21. Gupta, A., Hepp, B., and Khammash, M. (2016). Noise induces the population-level entrainment of incoherent, uncoupled intracellular oscillators. Cell Syst. *3*, 521-531.e13. 10.1016/j.cels.2016.10.006.

22. Mönke, G., Cristiano, E., Finzel, A., Friedrich, D., Herzel, H., Falcke, M., and Loewer, A. (2017). Excitability in the p53 network mediates robust signaling with tunable activation thresholds in single cells. Sci. Rep. 2017 71 *7*, 1–14. 10.1038/srep46571.

23. Kumpost, V., Hilbert, L., and Mikut, R. (2023). Noise facilitates entrainment of a population of uncoupled limit cycle oscillators. J. R. Soc. Interface *20*. 10.1098/rsif.2022.0781.

24. Venkatachalapathy, H., Azarin, S.M., and Sarkar, C.A. (2021). Trajectory-based energy landscapes of gene regulatory networks. Biophys. J. *120*, 687–698. 10.1016/j.bpj.2020.11.2279.

25. Venkatachalapathy, H., Brzakala, C., Batchelor, E., Azarin, S.M., and Sarkar, C.A. (2023). Inertial effect of cell state velocity on the quiescence-proliferation fate decision in breast cancer. 2023.05.22.541793. 10.1101/2023.05.22.541793.

26. Sheng, C., Mendler, I.H., Rieke, S., Snyder, P., Jentsch, M., Friedrich, D., Drossel, B., and Loewer, A. (2019). Pcna-mediated degradation of p21 coordinates the dna damage response and cell cycle regulation in individual cells. Cell Rep. *27*, 48-58.e7. 10.1016/j.celrep.2019.03.031.

27. Porter, J.R., Fisher, B.E., and Batchelor, E. (2016). P53 pulses diversify target gene expression dynamics in an mrna half-life-dependent manner and delineate co-regulated target gene subnetworks. Cell Syst. *2*, 272–282. 10.1016/j.cels.2016.03.006.

28. Jiménez, A., Lu, D., Kalocsay, M., Berberich, M.J., Balbi, P., Jambhekar, A., and Lahav, G. (2022). Time-series transcriptomics and proteomics reveal alternative modes to decode p53 oscillations. Mol. Syst. Biol. *18*, e10588. 10.15252/msb.202110588.

29. Hafner, A., Stewart-Ornstein, J., Purvis, J.E., Forrester, W.C., Bulyk, M.L., and Lahav, G. (2017). P53 pulses lead to distinct patterns of gene expression albeit similar DNA-binding dynamics. Nat. Struct. Mol. Biol. *24*, 840–847. 10.1038/nsmb.3452.

30. Reyes, J., Chen, J.-Y., Stewart-Ornstein, J., Karhohs, K.W., Mock, C.S., and Lahav, G. (2018). Fluctuations in p53 signaling allow escape from cell-cycle arrest. Mol. Cell *71*, 581-591.e5. 10.1016/j.molcel.2019.02.035.

31. Tsabar, M., Mock, C.S., Venkatachalam, V., Reyes, J., Karhohs, K.W., Oliver, T.G., Regev, A., Jambhekar, A., and Lahav, G. (2020). A switch in p53 dynamics marks cells that escape from dsb-induced cell cycle arrest. Cell Rep. *32*, 107995. 10.1016/j.celrep.2020.107995.

32. Abraham, U., Granada, A.E., Westermark, P.O., Heine, M., Kramer, A., and Herzel, H. (2010). Coupling governs entrainment range of circadian clocks. Mol. Syst. Biol. *6*. 10.1038/msb.2010.92.

33. Bordyugov, G., Granada, A.E., and Herzel, H. (2011). How coupling determines the entrainment of circadian clocks. Eur. Phys. J. B 2011 823 *82*, 227–234. 10.1140/epjb/e2011-20337-1.

34. Gu, C., Yang, H., Wang, M., and Rohling, J.H.T. (2019). Heterogeneity in relaxation rate improves the synchronization of oscillatory neurons in a model of the SCN. Chaos Interdiscip. J. Nonlinear Sci. *29*, 013103. 10.1063/1.5052299.

35. Geva-Zatorsky, N., Rosenfeld, N., Itzkovitz, S., Milo, R., Sigal, A., Dekel, E., Yarnitzky, T., Liron, Y., Polak, P., Lahav, G., et al. (2006). Oscillations and variability in the p53 system. Mol. Syst. Biol. *2*. 10.1038/msb4100068.

36. Batchelor, E., Mock, C.S., Bhan, I., Loewer, A., and Lahav, G. (2008). Recurrent initiation: a mechanism for triggering p53 pulses in response to dna damage. Mol. Cell *30*, 277–289. 10.1016/j.molcel.2008.03.016.

37. Gillespie, D.T. (1976). A general method for numerically simulating the stochastic time evolution of coupled chemical reactions. J. Comput. Phys. *22*, 403–434. 10.1016/0021-9991(76)90041-3.

38. Moser, J., Miller, I., Carter, D., and Spencer, S.L. (2018). Control of the restriction point by rb and p21. Proc. Natl. Acad. Sci. U. S. A. *115*, E8219–E8227. 10.1073/pnas.1722446115.

39. Regot, S., Hughey, J.J., Bajar, B.T., Carrasco, S., and Covert, M.W. (2014). High-sensitivity measurements of multiple kinase activities in live single cells. Cell *157*, 1724–1734. 10.1016/j.cell.2014.04.039.

40. Linkert, M., Rueden, C.T., Allan, C., Burel, J.M., Moore, W., Patterson, A., Loranger, B., Moore, J., Neves, C., MacDonald, D., et al. (2010). Metadata matters: access to image data in the real world. J. Cell Biol. *189*, 777–782. 10.1083/jcb.201004104.

Supplementary Material

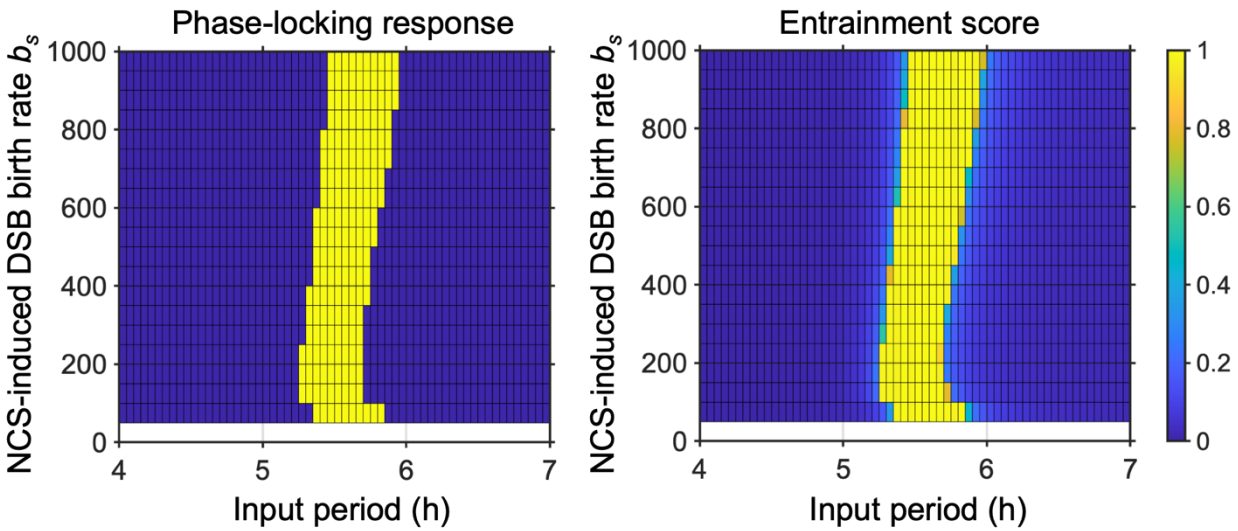

Figure S1: Phase-locking response and entrainment scores as a function of NCS-induced birth rate and input period. Yellow regions represent phase locking while blue represents no phase-locking.

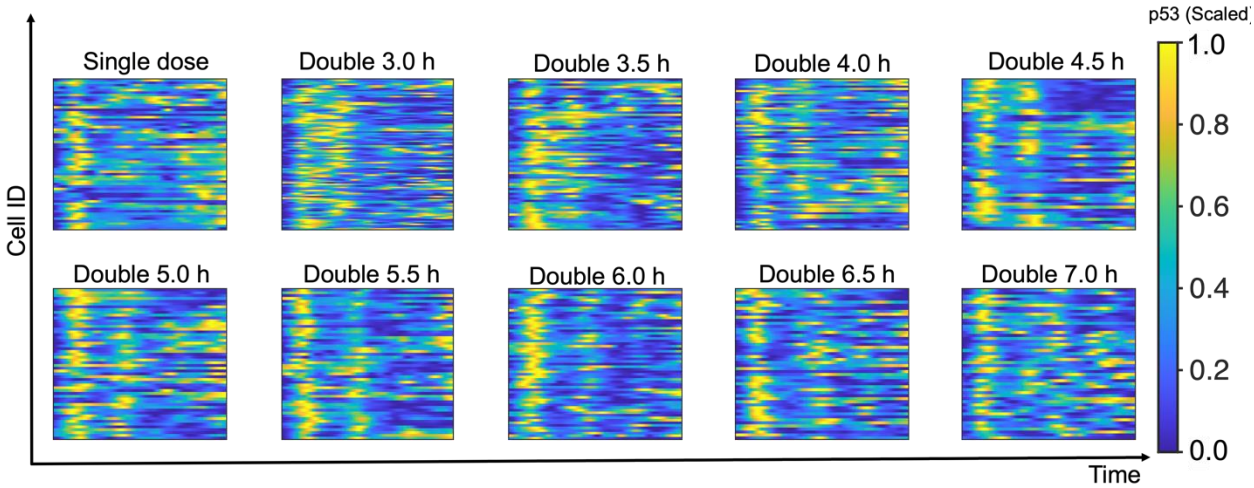

Figure S2: p53 responses from **Figures 1, 2** represented as a heat map diagram where each p53 trace is rescaled from 0 to 1.

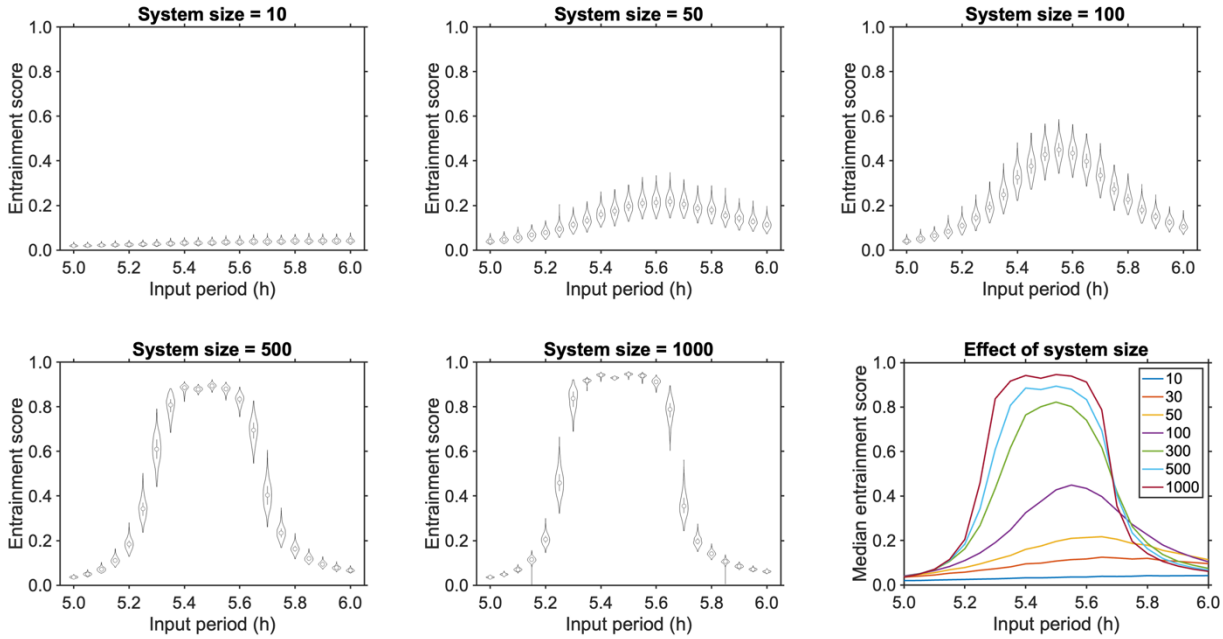

Figure S3: (A – E) Violin plots of the top 99% of entrainment scores for 1,000 realizations of the p53 DSB response in different system sizes at different NCS input periods for an NCS-induced break rate of 200 breaks/h. Here, system size refers to the factor used to convert concentration to number of molecules in the stochastic simulations. Larger system size implies more molecules and, therefore, less noise. Conversely, smaller system size implies fewer molecules and more noise. **(F)** Mean entrainment score of 1,000 realizations of the p53 DSB response in different system sizes at different NCS input periods for an NCS-induced break rate of 200 breaks/h. Overall, there is no increase in entrainment range due to intrinsic noise in comparison to the deterministic system.

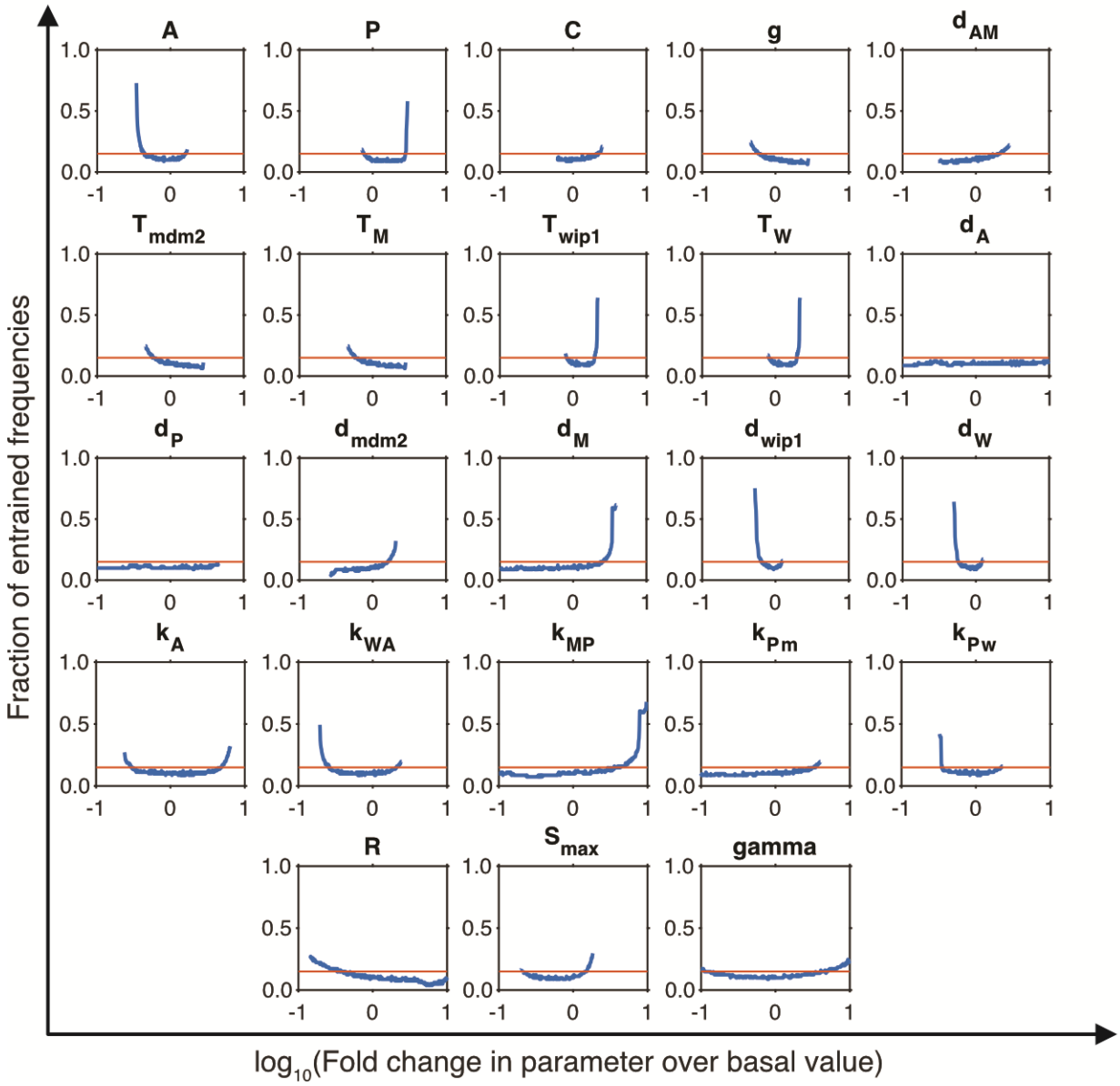

Figure S4: Effect of $\log_{10}$ fold-change in each parameter on the fraction of input periods in a scaled window around the natural oscillatory period of the system. Effect of parameters considered significant if the y-axis value exceeded 0.15 (orange line, ~50% increase over basal entrainment range). Explanation of symbols provided in **Table S1**.

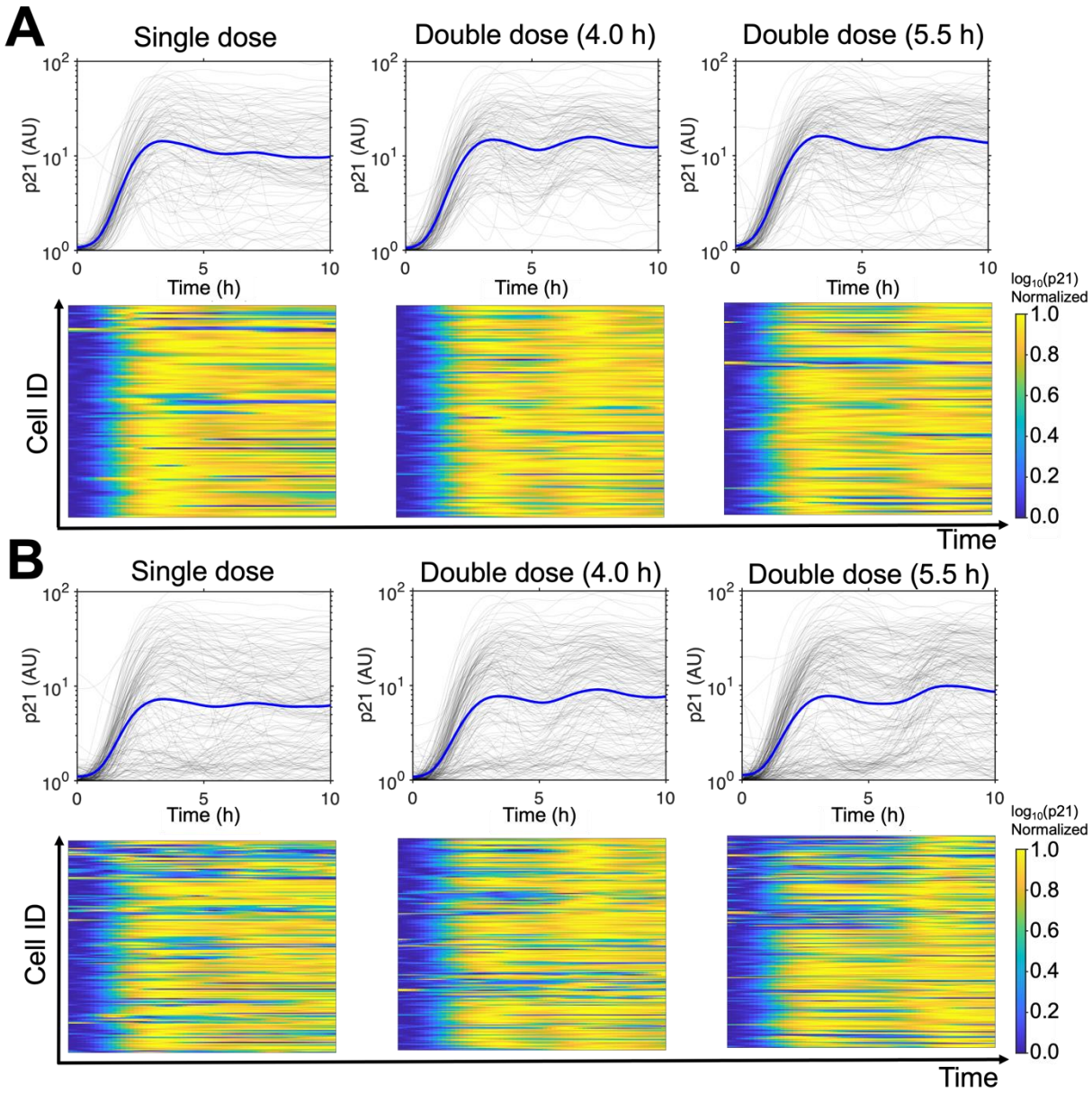

Figure S5: (A) Single-cell traces (gray) and mean p21 expression values (blue) for conditions from **Figure 4** along with a single dose of NCS as well as heat map diagrams for these conditions where each p21 trace is rescaled from 0 to 1. **(B)** All single-cell traces of p21 expression without filtering for responding cells showing variability in timing of p21 induction despite the same treatment conditions (as reported previously[26]).

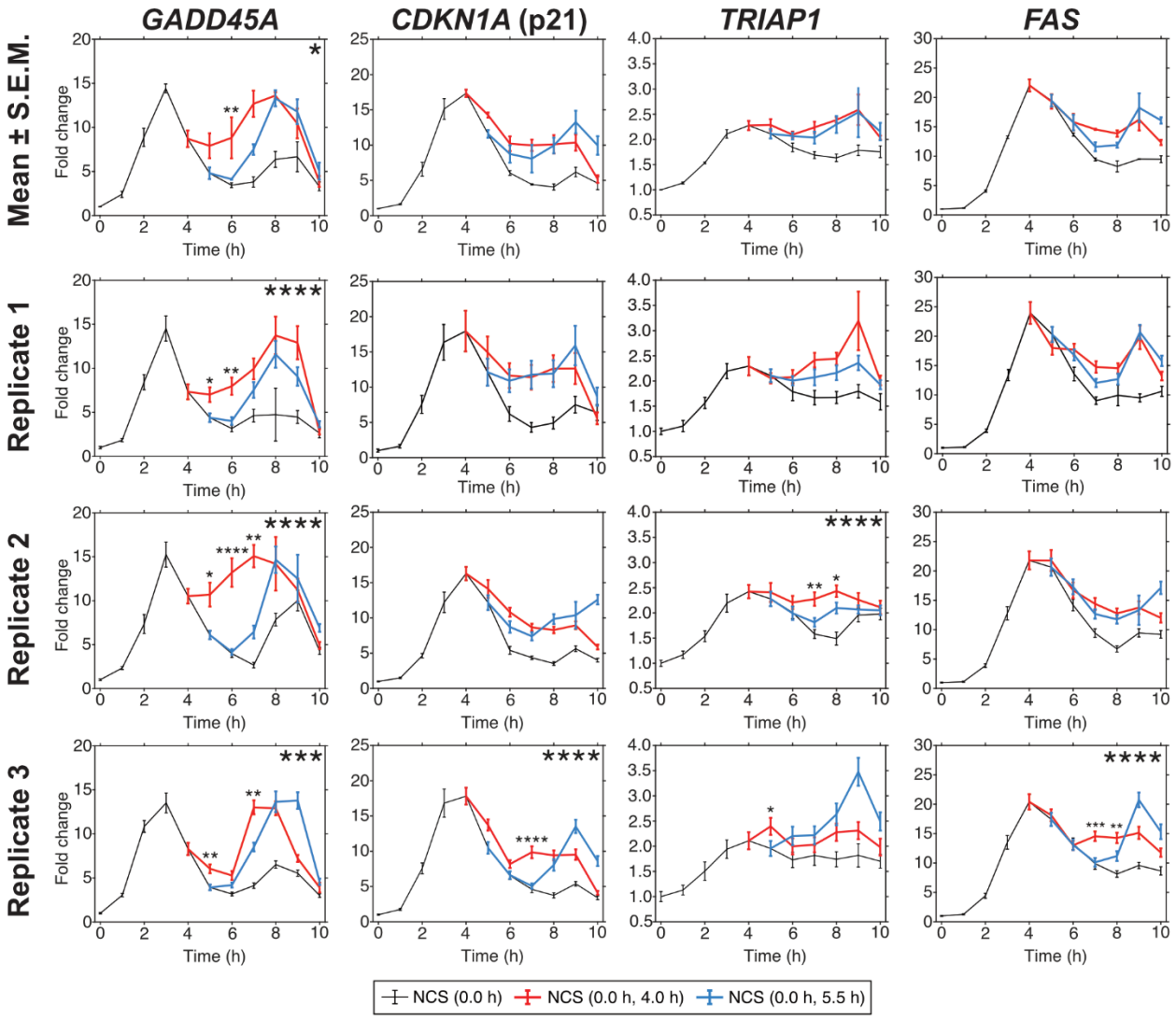

Figure S6: Gene expression of *GADD45A*, *CDKN1A*, *TRIAP1*, and *FAS* as measured by qRT-PCR in MCF-7 p53-mVenus cells treated with a single dose (black lines), or double dose of NCS at 4.0 h or 5.5 h intervals (red or blue lines, respectively). Top row is the mean and SEM of three biological replicates. Bottom rows show the mean and standard deviation of the technical replicates within each biological replicate. Statistical significance of the difference in gene expression between the 4.0 h treatment and 5.5 h treatment from 5.0 h to 8.0 h is shown on the top right of each plot. Statistical significance of the differences in gene expression at a specific time between the two conditions is shown on top of each point. (* $p < 0.05$; ** $p < 0.01$; *** $p < 0.001$; **** $p < 0.0001$)

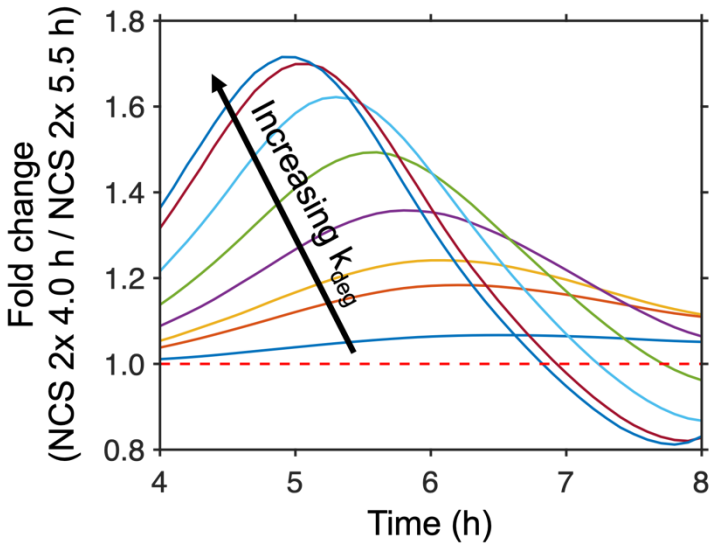

Figure S7: Mathematical modeling prediction of the fold change in mRNA expression with an NCS double dose in a 4.0 h interval compared to a 5.5 h interval for a range of mRNA degradation rates (k_{deg} = 0.01, 0.1, 0.2, 0.5, 1, 2, 5, and 10). Red dashed line represents no change.

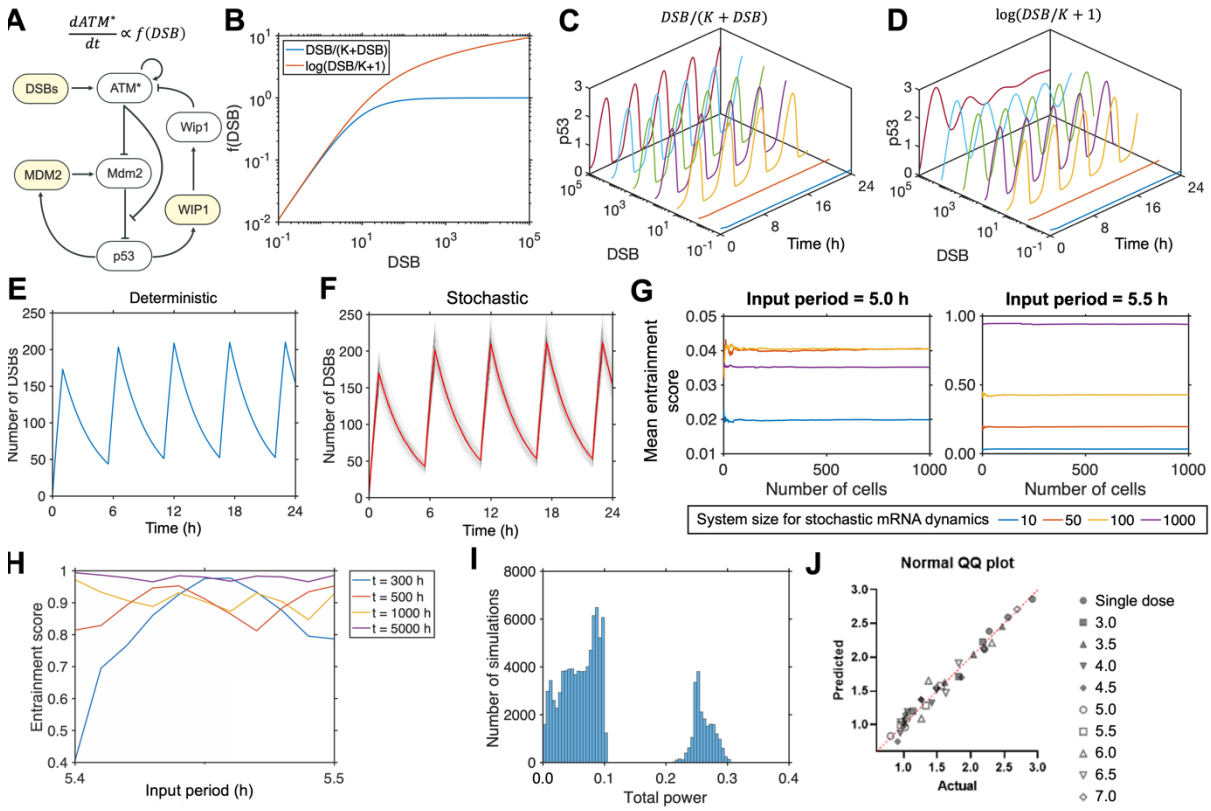

Figure S8: (A) Schematic of the p53 DSB response network where the rate of change in ATM* is directly proportional to a DSB input function **(B)** Plots of the saturable and non-saturable DSB input functions for different values of DSBs. **(C, D)** Simulations of the p53 system with the saturable **(C)** and non-saturable **(D)** DSB input functions for different values of DSBs showing similar behavior at low damage but divergent behavior at high damage. **(E)** Deterministic DSB induction and repair with NCS-induced damage being applied every 5.5 h with a NCS-induced birth rate of 200 breaks/h, showing a characteristic sawtooth shape. **(F)** Stochastic DSB inductions and repair with same conditions as (E). Gray lines represent individual realizations of the stochastic process; the red line represents the mean across multiple runs. **(G)** Plot showing the average entrainment score as a function of the number of stochastic realizations for a non-entraining and an entraining input period under different levels of noise. Each plot shows convergence well before 1,000 instances. **(H)** Entrainment score of the fully deterministic system for different simulation lengths showing fluctuations in shorter simulations due to the finite numerical nature of the DFT used to calculate the entrainment score. **(I)** Histogram of the total spectral power at steady state for systems with parameter sets randomly sampled in a 2-fold range around the basal values and simulated with 0 to 1,000 DSBs, in intervals of 20, as the input. **(J)** QQ plot of the Shapiro-Wilk normality test for data in **Figures 1, 2.**

Table S1. Parameter symbols and descriptions

Symbol	Parameter description	Value
A	ATM autophosphorylation rate	30.5
P	Wip1-dependent ATM dephosphorylation rate	22
C	Basal p53 synthesis rate	1.4
g	Mdm2-dependent p53 degradation rate	2.5
d_{AM}	ATM-dependent Mdm2 degradation rate	20
T_{mdm2}	MDM2 mRNA production rate	1.2
T_M	Mdm2 protein production rate	4
T_{wip1}	WIP1 mRNA production rate	1.2
T_W	Wip1 protein production rate	1
d_A	Basal ATM dephosphorylation rate	0.16
d_P	Basal p53 degradation rate	0.1
d_{mdm2}	MDM2 mRNA degradation rate	1
d_M	Mdm2 protein degradation rate	2
d_{wip1}	WIP1 mRNA degradation rate	1.3
d_W	Wip1 protein degradation rate	2.3
k_A	Michaelis constant for ATM autophosphorylation	0.5
k_{WA}	Michaelis constant for Wip1-dependent ATM dephosphorylation	0.14
k_{MP}	Michaelis constant for Mdm2-dependent p53 degradation	0.15
k_{Pm}	Michaelis constant for p53-dependent MDM2 mRNA production	1
k_{Pw}	Michaelis constant for p53-dependent WIP1 mRNA production	1
R	Strength of inhibition of Mdm2-dependent p53 degradation by ATM	2
S_{max}	Strength of ATM activation by DSBs	0.2
gamma	Michaelis constant of ATM activation by DSBs	9